





Cite this: DOI: 10.1039/d5gc00745c

Flash recovery of lithium from spent anode graphite by carbothermal shock and water leaching†

Duanmei Song, Beikai Zhang, Hongbiao Du, Jing Wu, Jiadong Yu * and Jinhui Li 

The global boom in electric vehicles has led to an alarming accumulation of lithium-ion battery waste. Battery recycling technologies have primarily focused on cathode metal recovery, while the contaminated anode graphite has been severely neglected. Conventional graphite recovery methods require multiple acid washes or prolonged high-temperature treatment and consume large amounts of energy and chemicals. Here, we develop an ultra-fast carbon thermal shock and water leaching (CTSW) method, which can transiently realize the complete stripping of anode materials, enable 100% recovery of graphite and copper foil, and recover valuable lithium resources. Specifically, carbon thermal shock (CTS) introducing auxiliary media (CaCO_3 , Al_2O_3 , etc.) promotes lithium aggregation from the interior to the surface of graphite, converts insoluble LiF to Li_2CO_3 , achieves deep leaching of >99.5% lithium, and immobilizes the hazardous byproduct, HF, to metal fluoride. Compared to conventional hydrometallurgy, LCA analysis shows that our CTSW method has a significantly lower environmental impact, energy, and cost.

Received 11th February 2025,
Accepted 9th May 2025

DOI: 10.1039/d5gc00745c

rsc.li/greenchem

Green foundation

1. This work proposed a flash carbothermal shock and Li extraction by clean water method. The recovery process produces no HF emissions, no wastewater, and low energy consumption.
2. Compared to conventional hydrometallurgy, LCA analysis shows that the method has reduced the GWP, acidification, and eutrophication potential by about 63.4%, human toxicity potential by 75.6%, and energy consumption by 70%.
3. Future work on studying the electrochemical properties of regenerated graphite, and on recycling the reaction medium for reuse.

1. Introduction

Graphite dominates the anode materials in commercialized lithium-ion batteries (LIBs) due to its low cost and excellent electrochemical properties, including good electrical conductivity, low operating voltage, high theoretical capacity, etc.¹ As the wave of LIB retiring from electric vehicles approaches, it is estimated that retired LIBs will generate approximately 4 million tons of spent graphite (SG) by 2030.² However, battery-grade graphite (>99.5%) production is still energy-intensive and highly polluting. Upgrading and recycling graphite from retired LIBs can significantly reduce the energy consumption, CO_2 , and pollution emissions of the traditional primary production process

while minimizing the release of hazardous substances, such as metals and electrolytes, from the graphite anode into the environment. Currently, the recycling of spent LIBs mainly focuses on recovering high-value cathode materials.³ In contrast, the resource utilization of anode materials is less emphasized, and SG is typically landfilled or incinerated.⁴ In traditional pyrometallurgy, SG can be a reductant for cathode valuable metal recovery,^{5,6} burning as fuel or ultimately being converted into slag, with low resource utilization. Meanwhile, the lithium content in anode SG is much higher than its abundance in the earth's crust (>3.007 wt% vs. 0.0017 wt%)⁷ and has a high recycling potential. As global resources are rapidly depleting, the deep recycling of valuable metals like lithium, current collector copper foil, and graphite from retired power batteries is crucial to prolonging their lifespan and better aligns with the principles of green chemistry^{8,9} and circular economy concepts.^{10,11}

Most methods for recovering lithium from graphite require prolonged roasting to remove the binder, followed by adding inorganic acids^{12,13} to leach the lithium from the graphite.

State Key Joint Laboratory Environmental Simulation & Pollution Control, School of Environment, Tsinghua University, Beijing 100084, China.

E-mail: yjd2022@tsinghua.edu.cn

† Electronic supplementary information (ESI) available. See DOI: <https://doi.org/10.1039/d5gc00745c>

That inevitably generates much energy consumption and secondary waste streams, resulting in a high environmental carbon footprint. Recently, the carbothermal shock (CTS) technology, which can achieve temperatures of thousands of degrees in an instant (0.01–2 s) using electrical pulses (heating rate $>1000\text{ }^{\circ}\text{C s}^{-1}$), has been hotly reported in fields like material synthesis,^{14,15} graphene preparation,^{16,17} and waste valorization.^{18,19} Zhang *et al.*²⁰ used shock heating (1500 $^{\circ}\text{C}$, 1 s) to achieve transient separation of anode graphite particles and copper current collectors, with a material recovery rate of 98.7% and nearly 100% integrity of the metal foil. Chen *et al.*²¹ employed an ultrafast flash evaporation method at 2850 K to decompose SEI resistance impurities. The anode graphite was regenerated after metal impurities were leached with dilute acid. However, the above methods focus on separating electrode materials or regenerating graphite under extremely high temperatures. They overlook the recovery of lithium, a key element in graphite (lithium volatilization temperature 700 $^{\circ}\text{C}$ –800 $^{\circ}\text{C}$), and the emission of toxic gases such as HF during CTS. By adding a specific alkaline auxiliary medium during the CTS process, the reaction temperature can be reduced, HF gas absorbed, and reactions between fluorine gases and electrode materials (metal oxides) prevented while also removing deep-seated fluorine that conventional pyrolysis cannot easily eliminate.^{7,22,23}

Metal oxides/hydroxides are effective for treating fluoridated wastewater, adsorbing fluoride through ion exchange, electrostatic attraction, chemical reaction, and pore filling to form metal fluorides.²⁴ However, metal oxide/hydroxide exhibits poor structural stability and is prone to leaching in water/acid, posing risks of secondary contamination and threats to human health.²⁵ Here, we introduced high-melting-point media (CaCO_3 , Al_2O_3 , Fe_2O_3), and proposed a media-assisted CTS strategy for battery anode components separation, lithium recovery, and fluorine fixation. Specifically, we employed a graphite boat as a heat transfer medium to deliver pulsed heat to the anode sheet and precisely control the temperature by adjusting current and time. The auxiliary media facilitate the separation of anode graphite from copper foil, the migration of lithium from the graphite interior to the surface, and *in situ* capture of fluorine-containing gases at high temperatures. After CTS, the anode sheet was easily separated from the media and effectively divided into graphite, copper foil, and lithium solution *via* ultrasonic treatment in water for 10 seconds without chemical reagents. Furthermore, we conducted a life cycle assessment (LCA) using Gabi software to compare the environmental impact of our method with conventional recycling methods. Compared to conventional pyrolysis (Table S1†), our method demonstrates exceptional efficiency and environmental friendliness, enabling instantaneous anode separation and efficient lithium extraction. That avoids the conventional steps of crushing, sieving, prolonged roasting, and acid leaching. And CTS consumes only 1/200 of the energy required by traditional tube furnaces (Table S2†), significantly reducing carbon emissions.

2. Experimental section

2.1 Materials and reagents

Ternary lithium batteries ($\text{LiNi}_{0.6}\text{Co}_{0.2}\text{Mn}_{0.2}\text{O}_2$, NCM) were purchased from a local electronic market in Shanghai, China. Sodium chloride (NaCl , AR; Sinopharm, Beijing, China), calcium carbonate (CaCO_3 , AR; Aladdin Biochemical Technology Co., Shanghai, China), aluminum oxide (Al_2O_3 , AR; Tongguang Fine Chemicals, Co., Beijing, China), ferric oxide (Fe_2O_3 , AR; Bor Chemicals Reagents Co., Shanghai, China), hydrochloric acid (HCl , AR; Tongguang Fine Chemicals, Co., Beijing, China), and nitric acid (HNO_3 , AR; Tongguang Fine Chemicals, Co., Beijing, China) were purchased from the unified reagent management platform of Tsinghua University. Solutions were prepared with deionized water by the laboratory water purification system (Medium-E600, Shanghai Hitech Instruments, Co., Shanghai, China).

2.2 CTS procedure

A flowchart comparison of the CTS and the traditional recycling method is shown in Fig. 1. The lithium battery pretreatment section is shown in Text S1.† First, the anode sheets of the disassembled spent ternary batteries were cut into $1 \times 1\text{ cm}^2$ pieces for later use. Then weigh the mass of the anode piece and weigh the auxiliary medium according to a specific mass ratio (auxiliary medium: anode piece mass ratio 1:1–5:1). Next, the auxiliary medium and anode piece were placed in a graphite boat, with the auxiliary medium covering both sides of the cathode, forming a sandwich-like structure. The anode sheet was Joule-heated through a connected power source, the heating temperature was adjusted by tuning the current (80–240 A), and the reaction time was set within 5–20 s.

2.3 Leaching procedure

The reacted anode piece buried in the powdered medium was carefully picked up with a tweezer, shaken gently to remove almost all of the medium, and placed into a small beaker containing deionized water. The anode piece was then subjected to ultrasonic treatment (40 W, 10 s). Lithium was selectively extracted from calcined graphite at room temperature with a simple water-leaching process. After filtration of the ultrasonic products, a lithium-containing solution, calcined graphite, and wholly stripped copper foil were obtained. The lithium solution was diluted to a fixed volume. ICP-OES measured the lithium concentration to calculate the lithium leaching rate. The stripped graphite residue and copper foil were collected, washed with clean water, dried at 60 $^{\circ}\text{C}$, and weighed, and the separation efficiency was calculated.

2.4 Analytical methods

The spent anode sheet raw material was placed in an ablation tank with aqua regia ($\text{HCl}/\text{HNO}_3 = 3:1$), digested and dissolved with the microwave ablation apparatus, and tested by ICP. ICP can measure the lithium concentration of the raw material C_0 . ICP can also measure the lithium-ion concen-

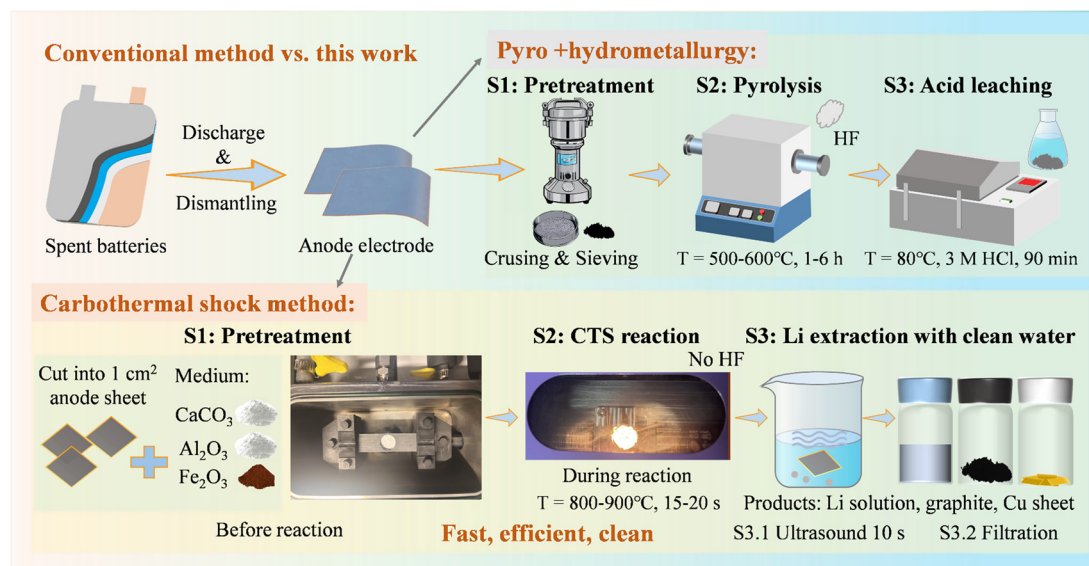


Fig. 1 Flowchart comparison of CTS and traditional recycling method.

tration of the leach solution after CTS and water leaching C_1 . Thus, the leaching rate of lithium ions (η) can be obtained according to eqn (1). In addition, to ensure the accuracy of the lithium leaching rate calculations and to identify possible lithium losses during the CTS process, the residue was also digested by acid to determine its lithium concentration by ICP.

$$\eta (\%) = C_1 V_1 / C_0 V_0 \times 100\% \quad (1)$$

Where C_1 is the concentration of Li in the leachate, V_1 is the volume of the leachate, C_0 is the concentration of Li in the raw material when digested in aqua regia, and V_0 is the volume of aqua regia leachate.

The anode sheets were weighed, placed in a crucible, and roasted in a tube furnace at 600 °C, 700 °C, and 800 °C for 1 h. The copper foil and graphite were completely separated, and the copper foil was weighed. Thus, the mass ratio of copper foil and graphite to the anode sheet was calculated, and the mass ratio of graphite was noted as a . The $1 \times 1 \text{ cm}^2$ anode sheet before CTS was weighed, and the mass was noted as M_0 . The mass of the copper foil after CTS, water immersion, and drying was noted as M_{Cu} . The separation efficiency of anode sheet graphite and copper foil was calculated by eqn (2).

$$\eta (\%) = (M_0 - M_{\text{Cu}}) / (M_0 \times a) \times 100\% \quad (2)$$

Where M_0 was the weighed mass of $1 \times 1 \text{ cm}^2$ anode electrode, M_{Cu} was the actual weight of the copper sheet obtained after CTS and water leaching, and a was the percentage of graphite in the anode electrode. All the results are measured three times and an average value was obtained through calculation.

2.5 Material characterization

The leaching concentration of Li ions using water was measured by inductively coupled plasma optical emission

spectrometry (ICP-OES, PerkinElmer, Avio 500, USA). The surface morphology and the elemental distribution of samples were characterized with scanning electron microscopy equipped with energy dispersive spectroscopy (SEM-EDS, Hitachi, SU-8010, Japan). The surface chemical composition and the variation of atomic proportion of elements at different depths of samples were measured by X-ray photoelectron spectroscopy (XPS, Thermo Fisher Scientific Inc, ESCALab Xi, USA). An estimated sputtering rate was 25 nm min^{-1} . Raman spectra were collected with a micro-Raman spectroscopy system (Renishaw, inVia Oontor, England) using a 532 nm laser with a power of 250 mW. The thermal process of samples was analyzed by thermal analysis of a combined system (TG-DSC/DTA-MS-FTIR, Netzsch, X70, Germany) from 30 to 1000 °C under Ar atmosphere. The samples' microscopic atomic arrangement and lattice evolution were carried out using the high-resolution field-emission transmission electron microscope (HRTEM, JEOL, JEM-2100F, Japan). Graphite particles were etched, and the corresponding time-of-flight secondary ion mass spectrometry spectra (TOF-SIMS, IONTOF GmbH, TOF. SIMS 5-100, Germany) and element distribution maps were acquired during etching to confirm the distributions of Li. An estimated sputtering rate was 1.47 nm s^{-1} . The crystal structures of the samples were characterized by X-ray diffraction (XRD, Bruker, D8 Advance, Germany) using a Cu K α radiation source ($\lambda = 0.154 \text{ nm}$) at 40 kV and 40 mA.

3. Results and discussion

3.1 CTS with medium promotes lithium leaching and material stripping

We have developed a simple CTS delamination and lithium extraction method with water. After the spent lithium batteries

were discharged and manually stripped, the anode material was obtained and cut into small fragments. We introduced an auxiliary medium for absorption and fixation to control fluorine emissions during the thermal decomposition of materials. The obtained anode piece and auxiliary medium were evenly placed in a Joule-heated graphite boat and calcined under an N_2 atmosphere (Fig. 2a). The heating temperature of the heater was controlled by adjusting the current (≈ 100 –240 A), as shown in Fig. 2b. In a typical CTS process, the heating element rises from room temperature to operating temperature within 1 s, followed by an isothermal period (5–20 seconds) and rapid cooling. The operating temperature of the heater increases with current, reaching over 1000 °C at 240 A, with energy consumption significantly lower than that of traditional high-temperature metallurgical processes. As shown in Fig. 2b and Fig. S1, Table S3,[†] adding the auxiliary medium

enhances the CTS process speed and stabilizes temperature control. That may be due to the auxiliary medium's heat storage and buffering effects, which reduce current-temperature control instability caused by variations between graphite boats.

We introduced metal oxides/hydroxides/carbonates as auxiliary media in CTS to facilitate binder decomposition and absorb HF gas. Low-melting-point auxiliary substances tend to melt during high-temperature CTS process, which is unfavorable for maintaining structural stability and separating the subsequent anode materials. Therefore, we selected auxiliary substances with high melting and boiling points (Table S4[†]) and anode sheet for co-carbon thermal shock. Fig. 2c and d showed the effects of different auxiliary media on the anode lithium leaching and material separation rates. Fig. 2e demonstrated the state of the anode sheet before and after CTS and

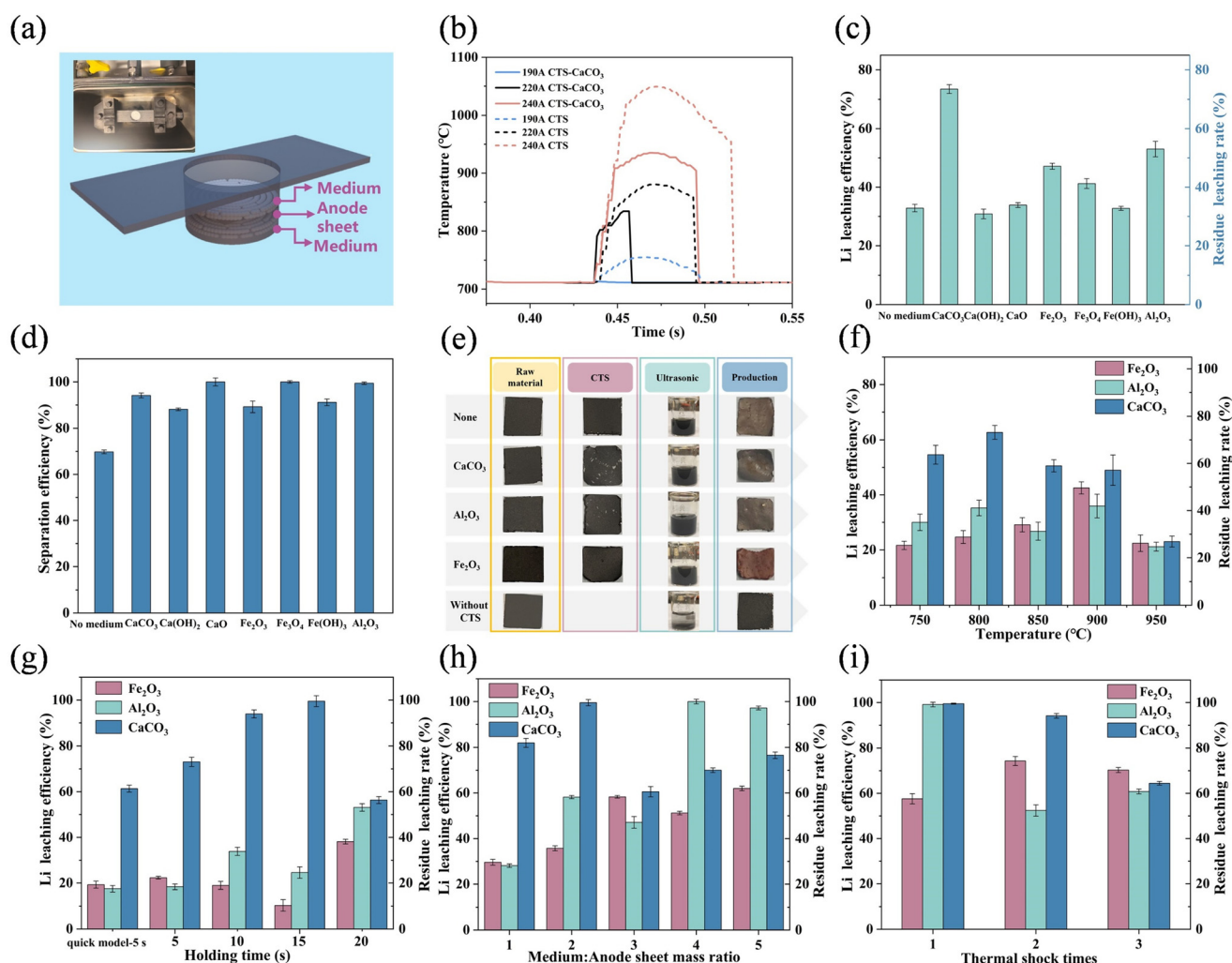


Fig. 2 Carbothermal shock separation of anode material and Cu foil. (a) Schematic illustration of the CTS process; (b) real-time temperature measurement under different currents (quick model, 5 s); (c) Li leaching efficiency under different auxiliary media; (d) separation efficiency of anode graphite and copper foil under different auxiliary media; (e) separation of anode graphite and copper foil without and with adding auxiliary media; (f) Li leaching efficiency under different temperatures; (g) Li leaching efficiency under different holding times; (h) Li leaching efficiency under different mass ratios of auxiliary medium and anode sheet; (i) Li leaching efficiency under different thermal shock times.

ultrasonication. The results suggested that adding auxiliary media significantly increased the anode material's lithium leaching and Cu foil separation efficiency compared to direct CTS. Besides, to ensure the leaching efficiency's accuracy and identify potential lithium losses during the CTS process, we determined the Li content of the residue. We found that the lithium loss rate was approximately 10% when direct CTS was conducted without adding an auxiliary medium. Whereas, after adding auxiliary media, the sum of lithium leaching by water and acid leaching from the residue is nearly 100%, and the lithium loss rate is negligible. That is consistent with the study of Zhang *et al.*²⁶ That was related to the fact that we covered the anode surface with sufficient medium, medium temperature, and short impact time. Adding an auxiliary medium greatly reduces lithium losses during heating processes. Finally, we selected CaCO_3 , Al_2O_3 , and Fe_2O_3 as the auxiliary media based on the lithium leaching enhancement effect.

To explore the optimal CTS process parameters, we analyzed the effects of different current intensities, retention times, auxiliary medium amounts, and shock counts on the lithium leaching efficiency of the anode material. We did not consider the effect of L/S during ultrasonic water leaching for the reasons given in Text S2.† The choice of medium significantly affects the leaching efficiency, with the highest lithium leaching efficiency achieved using the CaCO_3 medium (Fig. 2f). A moderate increase in temperature can increase the lithium leaching rate. However, excessively high temperatures will lead to lithium evaporation. A proper increase in retention time implies a longer reaction time, which can promote lithium leaching. However, if the reaction time is too long, lithium may evaporate from the graphite surface (Fig. 2g). Adequately increasing the amount of auxiliary medium can increase the lithium leaching efficiency (Fig. 2h), which can be attributed to the increased contact area between the auxiliary medium and the anode material. Increasing the number of thermal shocks can improve the heat conduction on the surface of the anode sheet, which may promote the accumulation of more lithium from within the graphite to the surface, thus enhancing the Li leaching efficiency under different media (Fig. 2i). Therefore, considering energy and time savings as well as high lithium leaching efficiency, the optimal CTS reaction temperature, time, mass ratio of medium to electrode material, and shock frequency with calcium carbonate medium are set as to be 800 °C, 15 s, 2 : 1, and 1 time, respectively, and the optimal lithium leaching rate was 99.5%. When aluminum oxide medium is added, the optimal CTS reaction temperature, time, mass ratio of medium to electrode material, and shock frequency are set to 900 °C, 20 s, 4 : 1, and 1 time, respectively, and the optimal lithium leaching rate was 99.2%. When the iron oxide medium is added, the optimal CTS reaction temperature, time, mass ratio of medium to electrode material, and shock frequency are set to 900 °C, 20 s, 5 : 1, and 2 times, respectively, and the optimal lithium leaching rate was 74.3%. The relevant experimental data and standard deviations are shown in Tables S5 and S6.†

3.2 CTS with medium promotes lithium aggregation on graphite surface

SEM analysis investigated material changes in the CTS and water-leaching process. As shown in Fig. 3a–h, compared to the case without additive (Fig. 3b), CTS with additive on the anode sheet results in the appearance of small particles on the heated spent graphite (HSG) surface, which disappear after water leaching and are likely lithium oxides.²⁷ During high-temperature evaporation of lithium²⁶ from the graphite interior under high-temperature thermal driving forces, experimental (Fig. 2c) and characterization analyses indicated that media addition could facilitate lithium diffusion to the surface, increasing the leaching rate. The rapid reaction and cooling led to lithium crystallization^{28,29} on the graphite surface, resulting in the formation of small particles during CTS with media addition, which were absent on the surface without media addition. The small particle sizes were captured and measured using Nano Measurer software, with sizes around 200–300 nm (Fig. 3i–l). The EDS spectra in Fig. 3m–o indicate that adding medium during CTS promotes complete separation of the anode copper foil from the graphite active material, achieving nearly 100% delamination rate (Fig. 3o), possibly because the medium acts as a heat reservoir.

To verify the hypothesis that the addition of auxiliary media facilitates lithium accumulation on the graphite surface, X-ray photoelectron spectroscopy (XPS) with varying etching times and TOF-SIMS were used for further validation. We etched the raw graphite spent material and the graphite particles subjected to CTS with added CaCO_3 medium (Fig. 4a–c). It was found that the characteristic lithium peak on the surface of graphite particles after CTS shifted significantly towards lower binding energies. Compared to SG, the graphite particles treated with CTS and CaCO_3 medium showed the highest surface atomic ratios of lithium and oxygen, gradually decreasing with etching depth. After CTS, the atomic ratio of fluorine remained very low compared to the raw material, indicating effective removal of F. TOF-SIMS further provided a clear and accurate analysis of the distribution of Li in SG, graphite after CTS, and water-leached residue (Fig. 4d–f). The lithium signal on the surface of the calcined graphite after CTS was robust, over twice the intensity of lithium on the surface of raw graphite. After water leaching, the lithium signal in the water-leached residue almost disappeared, indicating selective extraction of lithium into the aqueous solution through the CTS and water leaching method. The above further confirms that adding auxiliary media effectively promotes the migration of lithium within graphite to the surface, facilitating its extraction into an aqueous solution.

3.3 CTS with medium allows for HF fixation

We used XPS to characterize the chemical states of fluorine and metals (Ca, Al, Fe) in the medium after CTS to verify if the auxiliary medium could absorb fluorine. The F 1s XPS spectrum analysis (Fig. 5b) confirmed that fluorine was captured and fixed on the surface of the additive, resulting in metal fluorides. The Ca 2p spectrum (Fig. 5c) shows similar double peaks of Ca 2p_{3/2}

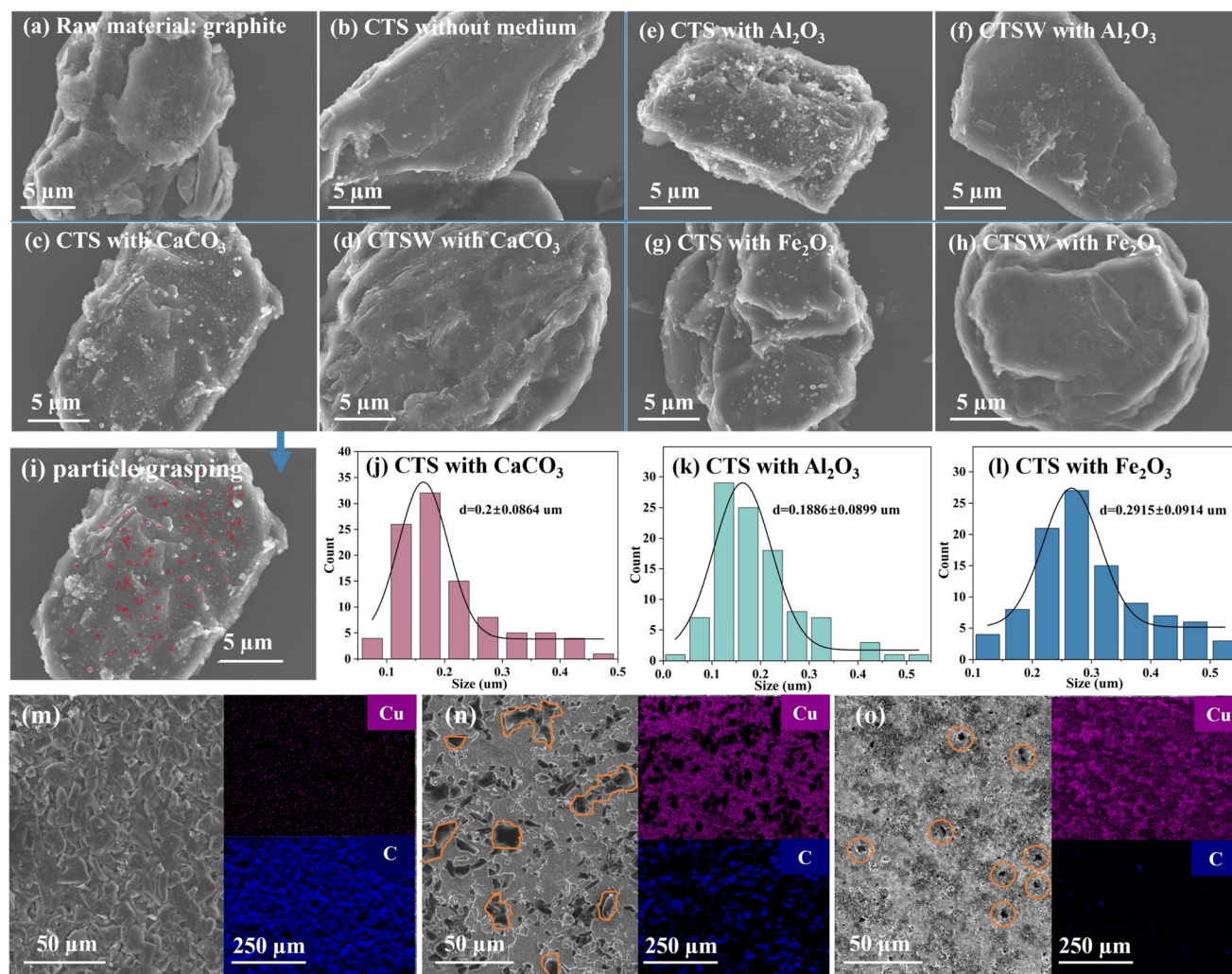


Fig. 3 (a) SEM image of raw spent graphite; (b) SEM image of HSG after CTS without medium; (c) SEM image of HSG after CTS with CaCO_3 medium; (d) SEM image of leaching residue after CTSW with CaCO_3 medium; (e) SEM image of HSG after CTS with Al_2O_3 medium; (f) SEM image of leaching residue after CTSW with Al_2O_3 medium; (g) SEM image of HSG after CTS with Fe_2O_3 medium; (h) SEM image of leaching residue after CTSW with Fe_2O_3 medium; (i) schematic diagram of capturing the small particles generated on the product surface after CTS added media using Nano Measurer software, with a size count of 100 small particles; (j–l) size distribution of small particles generated after CTS with CaCO_3 , Al_2O_3 and Fe_2O_3 media addition, respectively; (m) EDS image of raw anode material; (n) EDS image of copper foil after CTS without medium; (o) EDS image of copper foil after CTS with CaCO_3 medium.

and $\text{Ca } 2p_{1/2}$, a characteristic of Ca(II) oxidation states in calcium oxides. The broad prominent peak at 347.7 eV (FWHM 2.56 eV) is much broader than that of CaCO_3 (FWHM 1.8 eV (ref. 30)). That indicates that besides CaCO_3 , another Ca species, CaF_2 , is present, with a binding energy of 347.7 eV (followed by 351.1 eV). Within the 72–77 eV range, two signals correspond to the presence of Al^{3+} ions. The 74.6 eV signal is associated with the Al–O bond in Al_2O_3 , and the 75.1 eV signal is due to the Al–F bond in AlF_3 .³¹ The lower binding energy of Al–F may be due to the presence of a large number of oxygen atoms with lower electronegativity, which reduces the electron cloud density of AlF_3 and weakens the Al–F bond.³² The Al–F and Al–O bonds contribute 25.5% and 74.5%, respectively. Fe 2p XPS data show two peaks, where signals from 706 eV to 720 eV correspond to the Fe $2p_{3/2}$ peak, and binding energies from 720 eV to 733 eV

correspond to the Fe $2p_{1/2}$ peak. The peaks at 710.5 eV and 723.9 eV correspond to Fe_2O_3 , while binding energies at 718.5 and 732.7 eV are satellite peaks of high-spin Fe, and peaks at 713.0 eV and 727.2 eV are associated with FeF_3 .

Thermodynamic analysis suggests that in the <850 °C range, the Gibbs free energy change for reactions between HF and $\text{CaCO}_3/\text{Al}_2\text{O}_3$ is negative (Fig. 5d), indicating these fluorine-fixation reactions are thermodynamically favorable. Although thermodynamics predicts the Fe_2O_3 –HF reaction to occur below 400 °C, XPS analysis of metal fluoride formation suggests HF absorption can happen at low to moderate temperatures. For selecting fluorine-affine elements, we compared the ionization energies of different metals and the lattice energies of their fluorides, as seen in Table S7.† The ranking of metallic properties is $\text{Al} \approx \text{Ca} > \text{Fe}$. Fluorine has high electro-

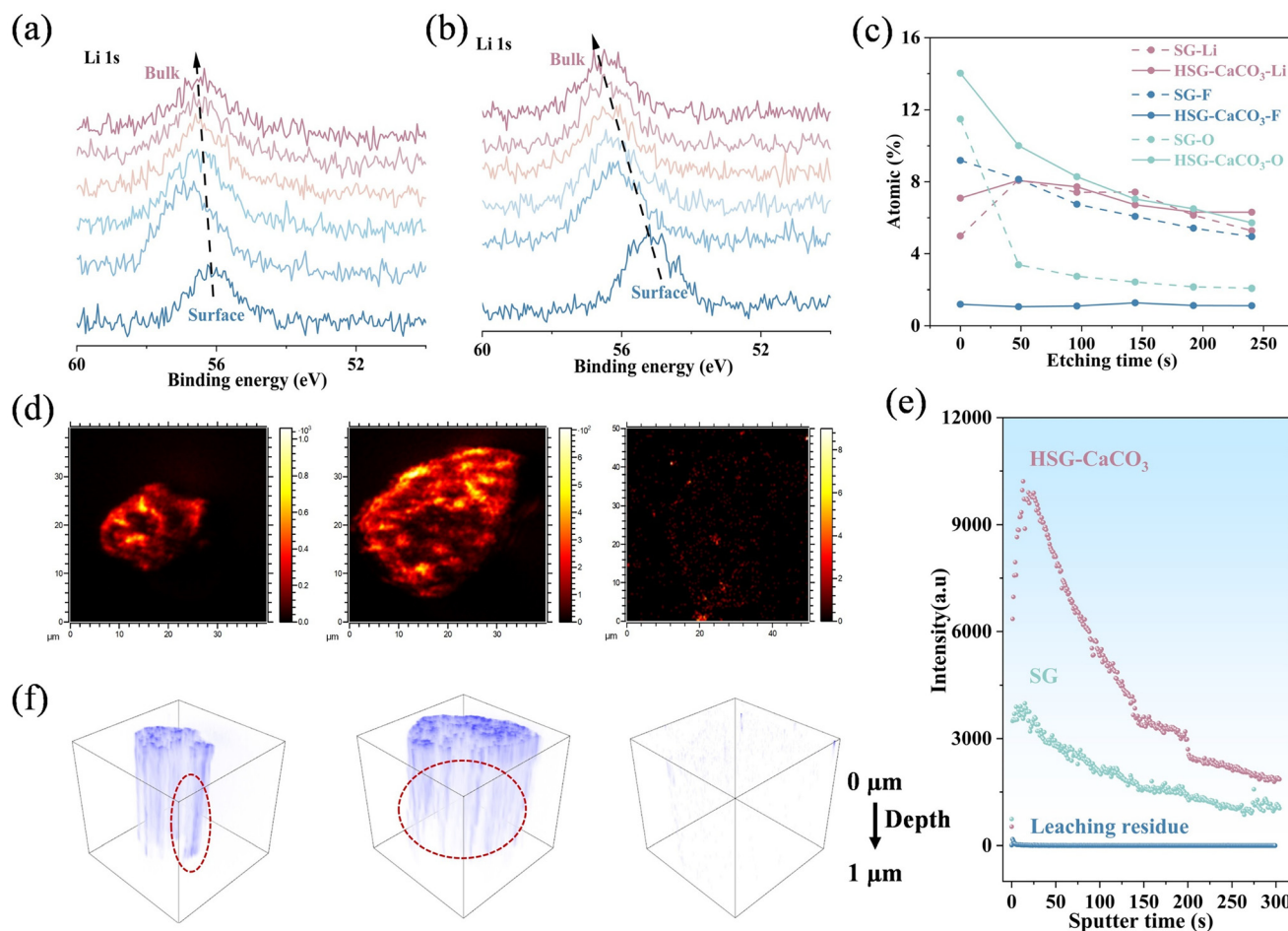


Fig. 4 XPS spectra of (a) SG raw material and (b) the sample after CTS with CaCO₃ medium under optimal conditions at various depths; (c) the variation curves of the atomic proportion of each element (Li, F, O) based on the analysis of XPS profiles at different depths; (d–f) TOF-SIMS mapping of SG, HSG (CTS with CaCO₃ medium) and leaching residue; (e) evolution with sputtering time of Li concentration in SG, HSG with CaCO₃ medium and leaching residue. An estimated sputtering rate was 24 nm min⁻¹.

negativity and is easily attracted to these metallic elements. Lattice energy quantifies the bonding strength between ions in ionic crystals, and aluminum, iron, and calcium strongly bond with fluoride ions. Overall, fluorine-affinitive elements Al and Ca outperform Fe, as supported by the fluorine content in the auxiliary medium after CTS (Table S8†).

To reveal the reaction mechanism of the auxiliary medium with pyrolysis gases, we further analyzed the gas evolution in the SG pyrolysis process. 3D Fourier transform infrared analysis showed characteristic infrared absorption peaks at each stage, revealing the primary pyrolysis gas products (Fig. 5a). Major observed products included gaseous components (CO₂, H₂O, and HF) and organic compounds (alkanes, alcohols, aldehydes, *etc.*).³³ The unique infrared absorption band at 2355 cm⁻¹ results from C=O stretching and bending vibrations, with CO₂ generated from the decomposition of carboxyl groups and esters. The characteristic peaks at 2250–2000 cm⁻¹ mainly represent C–O stretching vibrations, with CO generated by carbonyl groups and ether decomposition. In addition to gaseous components, C–H and C–O

stretching vibrations from organic compounds such as aldehydes, alcohols, and ketones were also detected. The absorption bands within 1900–1000 cm⁻¹ mainly correspond to organic components in pyrolysis gases, such as aldehydes, ketones, aromatic hydrocarbons, acids, alkanes, alcohols, phenols, esters, and related compounds.³⁴ TG-MS further investigated the gas release in the CTS process with and without added CaCO₃ medium (Fig. 5e). During pyrolysis in an N₂ atmosphere, typical gaseous products included hydrocarbons, carbonates, fluorinated acidic gases (HF, PF₅, and POF₃), and fluorinated hydrocarbons (fluoroethane, vinylidene fluoride, and 1,3,5-trifluorobenzene, *etc.*). During *in situ* pyrolysis, adding CaCO₃ as an auxiliary medium promotes the conversion of ketones into high-value gases such as alcohols and alkanes (Tables S9 and S10†).

3.4 Mechanical analysis

Unlike the cathode material of LIBs where the phase composition is easily determined, the anode graphite is difficult to analyze by XRD for very weak lithium species peaks due to the

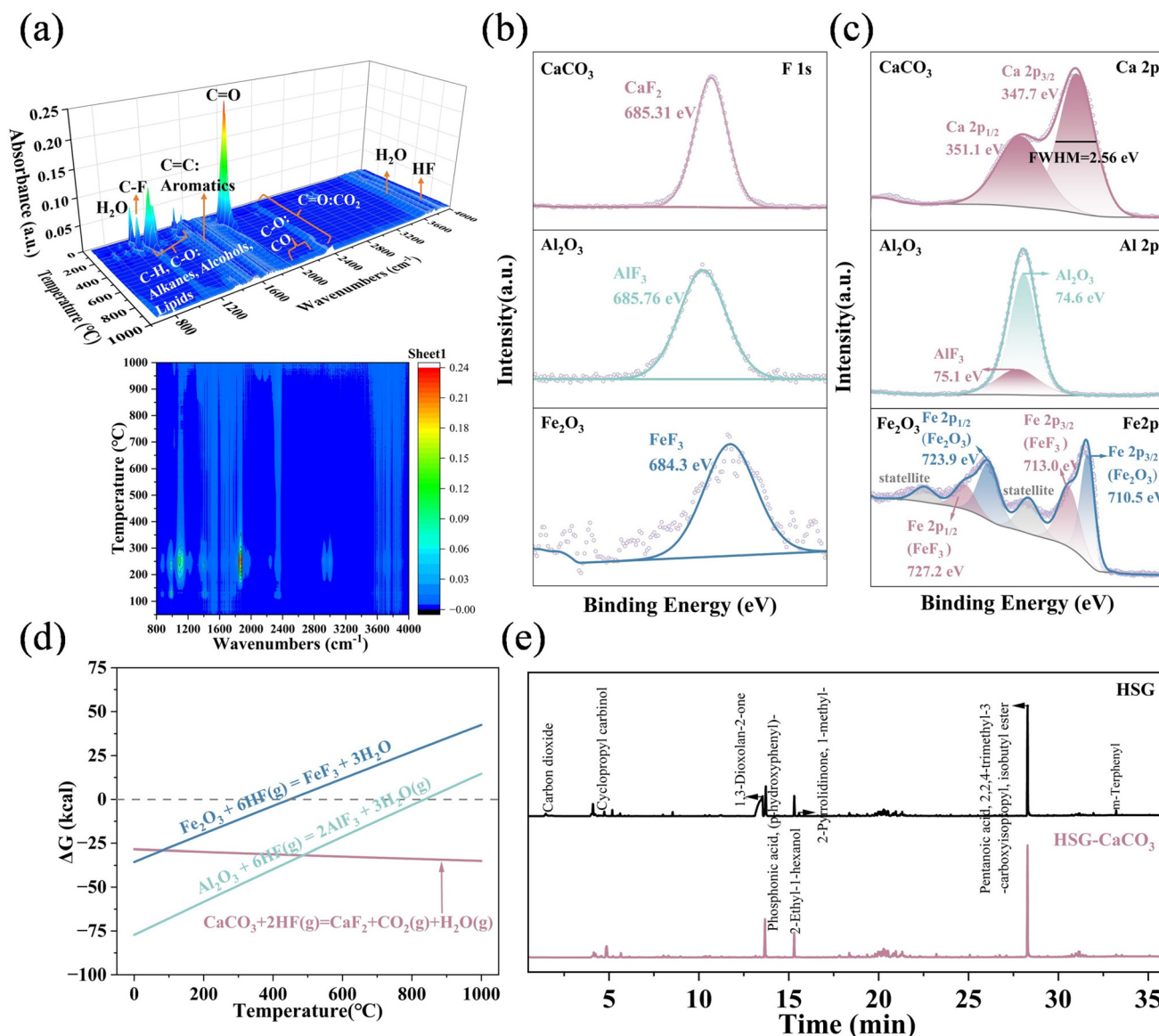


Fig. 5 (a) 3D-FTIR analysis from the pyrolysis of SG; (b) F 1s spectra and (c) M 2p (M represents metal such as Ca, Al, or Fe) spectra of the medium after CTS; (d) the Gibbs free energy change for reactions between HF and metal oxides, hydroxides was calculated using HSC 9.0 software; (e) TG-MS total ion current (TIC) profiles during the CTS process with and without CaCO₃ addition.

excessive intensity of the 002 peaks (Fig. S2†) and the low lithium content in graphite relative to the cathode. Therefore, we employed XPS analysis to characterize the chemical state of the elements on the surface of the sample and to study the changes in lithium species. We determined the lithium species by analyzing the Li 1s and O 1s of the sample before and after the CTS reaction, judging the elemental states based on the bond energies, and corroborating the two elements with each other.

As shown in Fig. 6a and b, the Li 1s spectra indicate that the lithium species in the raw material SG are Li₂CO₃ and LiF, which is consistent with the study of Yu *et al.*³⁵ LiF is a water-insoluble compound, challenging to leach from graphite with water. When CaCO₃ or Al₂O₃ was used as an auxiliary medium

during the CTS of the anode sheets, lithium on the graphite surface was present as Li₂CO₃, and the LiF in the raw material was converted to Li₂CO₃. That is because CaCO₃ or Al₂O₃ is thermodynamically more likely to react with LiF, forming metal fluorides and Li₂CO₃ (Fig. S3†). In contrast, adding Fe₂O₃ does not efficiently react with LiF in graphite, which explains the relatively low lithium leaching rate in carbothermal shock with Fe₂O₃. Li₂CO₃ is more soluble than LiF. According to the solubility parameter, the salts Li₂CO₃ (1.29 g/100 mL) and LiF (0.134 g/100 mL) are soluble in water at 25 °C, and the solubility increases with decreasing temperature.^{36,37} Theoretically, at room temperature, 25 mL of water is sufficient to fully dissolve Li₂CO₃ in hundreds of 1 cm² anode pieces (Text S2†), although we have the stereotypi-

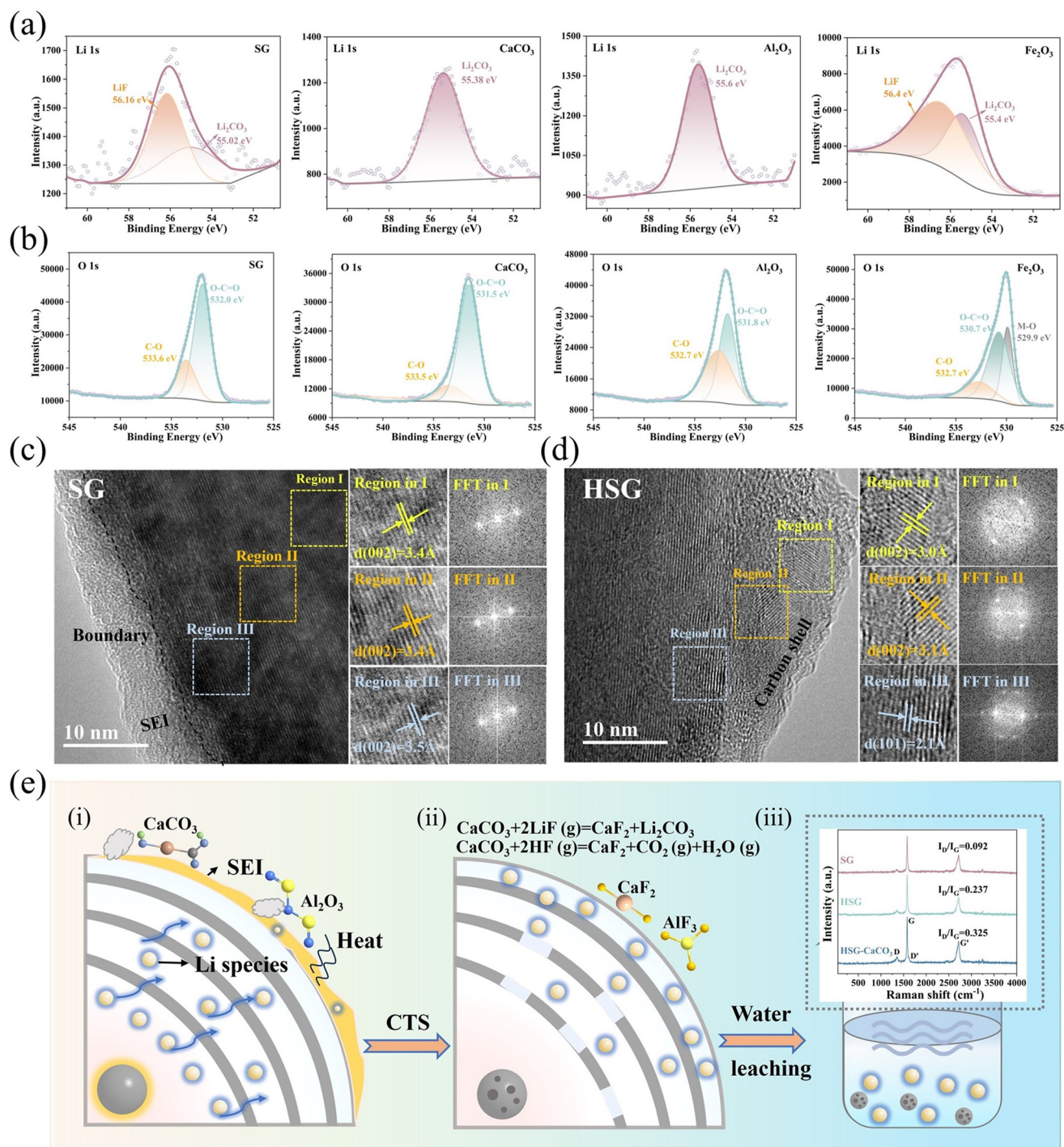


Fig. 6 XPS spectrum of SG and CTS-SG with a medium of (a) Li 1s and (b) O 1s. HTEM image of the (c) SG and (d) HSG with CaCO_3 medium. (e) Possible mechanisms, (i and ii) schematic diagram of spent graphite before and after CTS reaction, (iii) schematic diagram of lithium solution and graphite residue after water leaching.

cal impression that lithium carbonate is a precipitate. As a result, our work achieves a leaching rate of over 99%, compared to a lower lithium extraction rate of 81% to 85% by water leaching of LiF-containing samples by other researchers.^{38,39} The conversion of LiF to Li_2CO_3 realizes the

full recovery of lithium resources in graphite and deep defluorination.

To identify changes in the surface structure of the material, we further conducted high-resolution transmission electron microscopy (HR-TEM) observations on the microstructure of

SG and CTS-SG with CaCO_3 medium. Fig. 6c showed that the SG material surface is coated with solid-state electrolyte interface films (SEI). Below this layer, the graphite lattice edges are visible. The interlayer spacing is estimated to be about 3.4 Å, aligning with graphite's (002) crystal plane. Following CTS, the SEI layer thermally decomposes. Partial graphitization of carbon is observed, as shown in Fig. 6d. In Fig. 6d, region III, the 2.1 Å interplanar spacing corresponds to the (101) plane of graphite. The reduced spacing implies enhanced crystallinity of graphite after shock heating.²⁰ Fast Fourier transform (FFT) analysis shows a shift from linear to six-fold diffraction patterns along the [002] zone axis. That indicates that the single-layer graphite crystals transition to a complete hexagonal structure, demonstrating good graphite quality after CTS.

Based on SEM, XPS, Raman, thermodynamic calculations, and HTEM analysis results, the CTSW with auxiliary media and fluoride fixation mechanism is proposed, as shown in Fig. 6e. The high-temperature CTS process enables nearly complete separation of copper foil from graphite, binder decomposition on the graphite surface, and graphitization of the SEI film. The I_D/I_G ratio of HSG- CaCO_3 medium is 0.325, slightly higher than that of HSG without medium and SG. The struc-

ture of HSG- CaCO_3 is more disordered, possibly due to the heat retention effect of CaCO_3 promoting binder decomposition, leading to more defects. Lithium in graphite is mainly distributed within the SEI film and graphite pores. Adding auxiliary media causes lithium in the graphite to diffuse to the surface during evaporation and facilitates the transformation of less-soluble LiF on the SG material surface into Li_2CO_3 , thus improving lithium leaching rates. Additionally, the auxiliary medium absorbs and stabilizes HF by forming metal fluorides, preventing toxic gas formation and inhibiting the reaction between Li_2CO_3 in graphite and HF during pyrolysis, reducing lithium fluoride formation.

3.5 Life cycle assessment

Typically, spent lithium-ion batteries are firstly immersed in a 5 wt% NaCl solution or similar to achieve electrochemical discharge. Next, the discharged batteries are disassembled to separate the casing, separator, cathode, and anode components. The batteries are then mechanically shredded and sieved to obtain active material powder and collector fragments like Al and Cu. Our analysis begins with lithium battery discharge and excludes the cathode, separator, and other components.

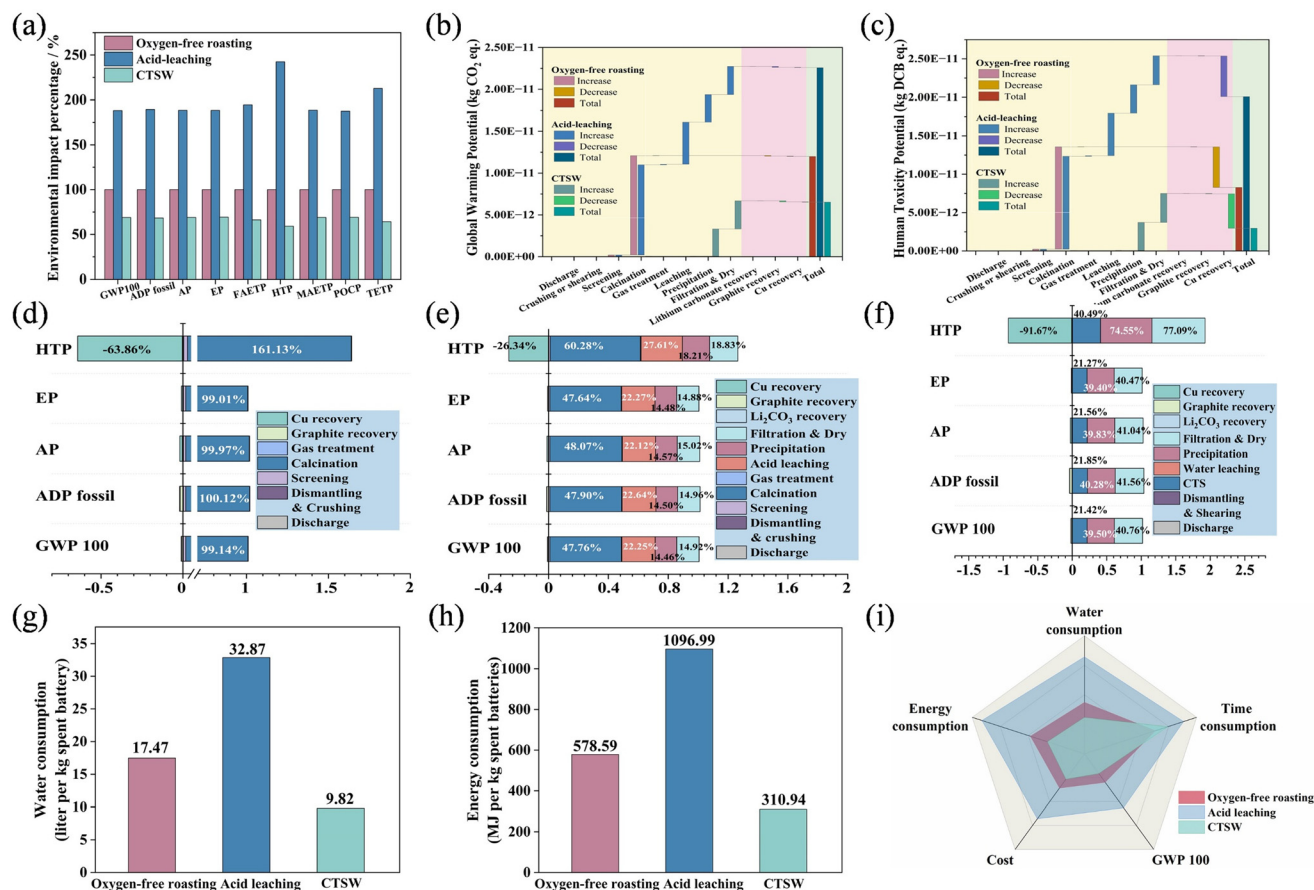


Fig. 7 Tech-economic analysis and environmental impact assessment of three graphite utilization methods. (a) Comparison of environmental impact analysis results among different processes; (b) global warming potential assessment; (c) human toxicity potential assessment; (d–f) key environmental impact analysis of major process steps in oxygen-free roasting, acid leaching, and CTSW; (g) comparison of water consumption; (h) comparison of energy consumption; (i) comprehensive comparisons of three utilization methods.

We consider only the material flow of the anode and focus solely on the environmental impact of graphite recovery. That makes the results valuable for quantitatively assessing SG utilization and guiding its recycling from lithium batteries. Based on published literature on graphite recovery, this paper uses Gabi software to analyze and compare traditional recovery methods' economic and environmental impacts and our work, including the oxygen-free roasting, acid leaching, and CTSW methods. We took 1 kg of spent lithium batteries as an example and illustrated the system boundaries in Fig. S4.† Details of the experimental data were shown in Tables S11–S13.†

Table S14† presents the overall environmental impact analysis results for oxygen-free roasting, acid leaching, and CTSW processes. We take the environmental impacts of oxygen-free roasting as 100%. Changes in various environmental indicators for different technologies were quantitatively compared, as shown in Fig. 7a. The cumulative ODP and ADP elements values for each recycling technology were too low for reliable comparison and were not analyzed. Overall, the environmental pollution emissions impact ranking for different SG utilization technologies is acid leaching highest, CTSW lowest. Acid leaching shows a more significant environmental impact than oxygen-free roasting due to additional steps such as leaching and precipitation. Additionally, this work analyzed the environmental impacts of different recycling steps using life cycle assessment, as shown in Tables S15–S17.† The study focused on five evaluation indicators closely related to emissions from lithium battery recycling. It normalized the environmental impact of each recycling stage with cumulative effects, as illustrated in Fig. 7b–f and Fig. S4.† The findings reveal that high-temperature calcination/drying and chemical reagent use are critical contributors to environmental impact. Since the oxygen-free roasting technology does not involve subsequent lithium extraction, CTSW technology is mainly compared with traditional acid leaching. Compared with traditional acid leaching, the new technology reduces global warming, acidification, and eutrophication potential by about 63.4% and human toxicity potential by 75.6%. Due to ultra-short reaction times and high energy efficiency, CTSW's water and energy consumption are also significantly reduced by 70% (Fig. 7g and h), achieved through optimizing thermal treatment duration and leaching processes. Compared to acid leaching, the cost of processing about 0.2 kg of anode material (from 1 kg lithium batteries) is approximately 60.8% lower (Table S15†). Overall, CTSW technology shows marked advantages over conventional acid leaching in water and energy consumption, cost, global warming potential, and processing time (Fig. 7i).

4. Conclusion

The alkaline media-assisted CTS method has proven an effective way to recover lithium, copper foil, and graphite from spent lithium battery anodes. Unlike direct carbon thermal

shock, the assisted medium reacts with water-insoluble LiF to produce metal fluoride and Li_2CO_3 , allowing for deep lithium recovery from graphite and immobilization of the HF gas generated during the high-temperature process. As a result, the leaching efficiency of lithium exceeds 99% using a combination of auxiliary media roasting and clean water leaching methods. The recovered lithium, graphite, and copper foil can be used as a secondary resource in the supply chain to manufacture new batteries. The recovery process produces no HF emissions, no wastewater, and low energy consumption. Compared to conventional hydrometallurgy, LCA analysis shows that the CTSW method has reduced the GWP, acidification, and eutrophication potential by about 63.4%, human toxicity potential by 75.6%, and energy consumption by 70%. The technology efficiently recovers all components in anode materials, offering low energy consumption and eco-friendly benefits. The scale-up of graphene synthesis *via* transient thermal processes has reached production rates of several tons per day in 2024. This established scalability can be easily used in this study. The clean and efficient CTS method could make the battery recycling industry a prime example of circular economy and cleaner production.

Author contributions

Duanmei Song: conceptualization, data curation, methodology, writing original draft. Beikai Zhang: methodology, review & editing. Hongbiao Du: formal analysis, review & editing. Jing Wu: formal analysis, review & editing. Jiadong Yu: review & editing, supervision. Jinhui Li: supervision, funding acquisition.

Data availability

All the data provided in this article are included within the figures and tables of this article and the ESI.†

Conflicts of interest

The authors declare that they have no known competing financial interests or personal relationships that could have appeared to influence the work reported in this paper.

Acknowledgements

This work was supported by financial support by the National Natural Science Foundation of China (52300162, Y. J. D. and 52270127, L. J. H.). The financial support for this project comes from legal channels.

References

- 1 J. Wu, M. Zheng, T. Liu, Y. Wang, Y. Liu, J. Nai, L. Zhang, S. Zhang and X. Tao, *Energy Storage Mater.*, 2023, **54**, 120–134.
- 2 D. Song, J. Yu, J. Wu, B. Zhang and J. Li, *J. Cleaner Prod.*, 2025, **486**, 144495.
- 3 P. Jenis, T. Zhang, B. Ramasubramanian, S. Lin, P. R. Rayavarapu, J. Yu and S. Ramakrishna, *Circ. Econ.*, 2024, **3**, 100087.
- 4 M. Kaya, *Circ. Econ.*, 2022, **1**, 100015.
- 5 C. Pan and Y. Shen, *J. Energy Chem.*, 2023, **85**, 547–561.
- 6 C. Yang, J. Zhang, Y. Chen and C. Wang, *J. Power Sources*, 2023, **584**, 233611.
- 7 D. Liu, X. Qu, B. Zhang, J. Zhao, H. Xie and H. Yin, *ACS Sustainable Chem. Eng.*, 2022, **10**, 5739–5747.
- 8 J. B. Zimmerman, P. T. Anastas, H. C. Erythropel and W. Leitner, *Science*, 2020, **367**, 397–400.
- 9 D. Song, J. Yu, M. Wang, Q. Tan, K. Liu and J. Li, *Energy Storage Mater.*, 2023, **61**, 102870.
- 10 K. Liu, Q. Tan, J. Yu and M. Wang, *Circ. Econ.*, 2023, **2**, 100028.
- 11 J. Li and G. Xu, *Circ. Econ.*, 2022, **1**, 100002.
- 12 D. Yang, Y. Yang, H. Du, Y. Ji, M. Ma, Y. Pan, X. Qi, Q. Sun, K. Shi and L. Qie, *Green Energy Environ.*, 2024, **9**, 1027–1034.
- 13 Y. Guo, F. Li, H. Zhu, G. Li, J. Huang and W. He, *Waste Manage.*, 2016, **51**, 227–233.
- 14 F. Yu, C. Jia, X. Wu, L. Sun, Z. Shi, T. Teng, L. Lin, Z. He, J. Gao, S. Zhang, L. Wang, S. Wang and X. Zhu, *Nat. Commun.*, 2023, **14**, 4975.
- 15 K. M. Wyss, J. T. Li, P. A. Advincula, K. V. Bets, W. Chen, L. Eddy, K. J. Silva, J. L. Beckham, J. Chen, W. Meng, B. Deng, S. Nagarajaiah, B. I. Yakobson and J. M. Tour, *Adv. Mater.*, 2023, **35**, 2209621.
- 16 D. X. Luong, K. V. Bets, W. A. Algozeeb, M. G. Stanford, C. Kittrell, W. Chen, R. V. Salvatierra, M. Ren, E. A. McHugh, P. A. Advincula, Z. Wang, M. Bhatt, H. Guo, V. Mancevski, R. Shahsavari, B. I. Yakobson and J. M. Tour, *Nature*, 2020, **577**, 647–651.
- 17 K. M. Wyss, W. Chen, J. L. Beckham, P. E. Savas and J. M. Tour, *ACS Nano*, 2022, **16**, 7804–7815.
- 18 Y. Cheng, J. Chen, B. Deng, W. Chen, K. J. Silva, L. Eddy, G. Wu, Y. Chen, B. Li, C. Kittrell, S. Xu, T. Si, A. A. Martí, B. I. Yakobson, Y. Zhao and J. M. Tour, *Nat. Sustainability*, 2024, **7**, 452–462.
- 19 B. Deng, X. Wang, D. X. Luong, R. A. Carter, Z. Wang, M. B. Tomson and J. M. Tour, *Sci. Adv.*, 2022, **8**, eabm3132.
- 20 H. Zhang, Y. Ji, Y. Yao, L. Qie, Z. Cheng, Z. Ma, X. Qian, R. Yang, C. Li, Y. Guo, Y. Yuan, H. Xiao, H. Yang, J. Ma, J. Lu and Y. Huang, *Energy Environ. Sci.*, 2023, **16**, 2561–2571.
- 21 W. Chen, R. V. Salvatierra, J. T. Li, C. Kittrell, J. L. Beckham, K. M. Wyss, N. La, P. E. Savas, C. Ge, P. A. Advincula, P. Scotland, L. Eddy, B. Deng, Z. Yuan and J. M. Tour, *Adv. Mater.*, 2023, **35**, e2207303.
- 22 M. Wang, Q. Tan, L. Liu and J. Li, *ACS Sustainable Chem. Eng.*, 2019, **7**, 12799–12806.
- 23 H. Huang, C. Liu and Z. Sun, *J. Hazard. Mater.*, 2023, **457**, 131782.
- 24 Y. Wei, L. Wang, H. Li, W. Yan and J. Feng, *Front. Chem.*, 2022, **10**, 900660.
- 25 J. Lin, Y. Chen, X. Hong and C. Huang, *J. Colloid Interface Sci.*, 2020, **561**, 275–286.
- 26 B. Zhang, L. Wang, D. Song, J. Wu, J. Yu and J. Li, *Chem. Eng. J.*, 2025, **505**, 159206.
- 27 X. H. Zhu, Y. J. Li, M. Q. Gong, R. Mo, S. Y. Luo, X. Yan and S. Yang, *Angew. Chem., Int. Ed.*, 2023, **62**, e202300074.
- 28 B. Nicolas, G. Nathanael, A.-O. Duangdao and S. Nicolas, *J. Phys. Chem. C*, 2017, **121**, 11915–11925.
- 29 J. Zou, L. Tang and L. Kang, *ACS Nano*, 2025, **19**, 152–186.
- 30 S. Budyanto, Y. L. Kuo and J. C. Liu, *Sep. Purif. Technol.*, 2015, **150**, 325–331.
- 31 K. Milewska, M. Maciejewski, M. Łapiński, A. Synak, M. Behrendt, W. Sadowski and B. Kościelska, *J. Non-Cryst. Solids*, 2023, **605**, 122169.
- 32 T. Chen, H. Liu, M. Sun, B. Yang, P. Ning, X. Zhu, S. V. Savilov, S. M. Aldoshin, J. Xu and H. Xia, *Energy Fuels*, 2024, **38**, 12239–12250.
- 33 F. Zhou, H. Wang, S. Wang, J. Zhao, X. Qu, D. Wang, Y. Cai, Z. Zheng, D. Wang and H. Yin, *Environ. Sci. Technol.*, 2024, **58**, 2102–2111.
- 34 F. Ullah, G. Ji, L. Zhang, M. Irfan, Z. Fu, Z. Manzoor and A. Li, *Chem. Eng. J.*, 2023, **473**, 145300.
- 35 J. Yu, M. Lin, Q. Tan and J. Li, *J. Hazard. Mater.*, 2021, **401**, 123715.
- 36 C. B. Stubblefield and R. O. Bach, *J. Chem. Eng. Data*, 1972, **17**, 491–492.
- 37 H. Feuer, *Science*, 1954, **119**, 1254.
- 38 G. Zhang, Z. Liu, X. Yuan, Y. He, N. Wei, H. Wang and B. Zhang, *J. Hazard. Mater.*, 2022, **430**, 128374.
- 39 W. Ding, S. Bao, Y. Zhang, L. Ren, C. Xin, B. Chen, B. Liu, J. Xiao and X. Hou, *Green Chem.*, 2023, **25**, 6652–6665.